

Synthesis and Photocatalytic Activity of Zinc and Tungsten Co-Doped Barium Titanate Perovskite for Methylene Blue Degradation under Solar Irradiation

¹Hayet Menasra*, ²Fatima Adjal, ³Chaima Benbrika, ⁴Lakhdar Smaili, ⁵Karima Bounab
⁶Zelikha Necira and ⁷Amara Elfetni

^{1, 4, 7} University of Biskra, BP 145 RP, Biskra 07000, Departement of of Industrial Chemistry,
Laboratory of Applied Chemistry (Algeria).

³University of Biskra, BP 145 RP, Biskra 07000, Departement of of Industrial Chemistry, (Algeria).

^{2, 5, 6} University of Biskra, BP 145 RP, Biskra 07000, Departement of Science of Matter, Laboratory of
Applied Chemistry (Algeria).
h.menasra@univ-biskra.dz*

(Received on 11th September 2023, accepted in revised form 11th December 2023)

Summary: This research delves into the properties of x% ZW-BT compounds (x=3% and 7%), synthesized using a solid-state reaction approach. Utilizing X-ray diffraction, the crystal structure of the x% ZW-BT compositions is confirmed, showcasing a distinct tetragonal symmetry devoid of any parasitic phases. With increasing dopant concentrations, slight reductions in lattice parameters are observed, signifying the even diffusion of dopant (Zn^{2+} and W^{6+}) ions. Moreover, the validation of metal-oxygen bonding vibrations is achieved through Fourier-transform infrared spectroscopy (FTIR) analysis. Scanning electron microscopy (SEM) coupled with energy-dispersive X-ray spectroscopy (EDX) reveals consistent granular arrangements and clear elemental signatures in both compositions. Notably, photocatalytic experiments highlight remarkable degradation rates; within 100 minutes, 3% and 7% ZW-BT achieve degradation levels of 78.04% and 88.9% respectively. These findings underscore the significant potential of these compounds for environmentally friendly photocatalytic applications.

Keywords: Perovskite; Doped BaTiO₃; Metal-O vibration; Catalyst; Methylene bleu dye.

Introduction

In recent years, perovskite-based materials have garnered significant attention due to their exceptional properties and potential applications across various scientific and technological fields [1]. Among these perovskites, BaTiO₃, known as barium titanate, stands out for its remarkable ferroelectric [2], piezoelectric [3], and optical [4] properties. These attributes make it a prime candidate for a diverse range of applications, spanning from electro-optic devices to photocatalytic catalysts [5,6].

However, ongoing research seeks methods to enhance the performance and functionalities of perovskites, and chemical doping has emerged as a promising strategy to achieve this aim. Controlled incorporation of dopant elements into the crystal structure of BaTiO₃ perovskites (of the ABO₃ type), either at the A-site [7] or B-site [8], guided by the ionic radii of these elements and their impact on structural stability, can lead to significant modifications in electrical [9] and catalytic [5,10] properties. The nature of the dopant influences the crystal structure of BT perovskite, adopting a tetragonal structure at low concentrations (< 2%) [11] and a cubic structure at higher concentrations [12], or coexisting with an

orthorhombic phase in the case of random doping involving transition metals and rare earths [13,14].

Furthermore, the dopant's nature affects BT grain structure's density and growth, as observed with Zn^{2+} and W^{6+} ions, which are employed in ferroelectric [15], photocatalytic [16] and radiation shielding [17] applications. A specific dopant combination, (Zn_{1/2}, W_{1/2}), in BT perovskite, has attracted significant attention in the field of ferroelectric materials, as shown by the research conducted by Cailan Tian *et al.* [13]. They varied the dopant concentration from 40 to 100% to examine its impact on microwave dielectric properties.

Moreover, employing BaTiO₃ perovskite doped with the (Zn_{1/2}, W_{1/2}) combination offers novel pathways for photocatalytic applications, representing an innovative, environmentally conscious method for degrading organic pollutants. In this context, our study focuses on methylene blue degradation under solar irradiation, employing Ba (Zn_{1/2}, W_{1/2})_xTi_(1-x)O₃ perovskite (with x= 3% and 7%). These materials are synthesized using the solid–solid method and

*To whom all correspondence should be addressed.

characterized through XRD, FTIR, SEM/ EDX, and UV-visible spectroscopy.

Experimental

The solid-solid process was selected for synthesizing $\text{Ba}(\text{Zn}_{1/2}, \text{W}_{1/2})_x\text{Ti}_{(1-x)}\text{O}_3$ perovskite, denoted as $x\%$ ZW-BT, with varying compositions of $x = 3$ and 7% . High-purity precursors, including BaCO_3 (95 %, BIOCHEM), WO_3 (99.9%, Alfa Aesar), ZnO (99.99 %, Alfa Aesar), and TiO_2 (99 %, BIOCHEM), were manually ground for 4 hours. The resulting mixture was then subjected to calcination at 950°C for 4 hours, with a heating rate of $2^\circ\text{C}/\text{min}$. Following this, an additional grinding step for 4 hours was performed, followed by a second calcination at the same temperature of 950°C , aimed at preventing the formation of any parasitic phases [18]. Subsequently, the resulting material underwent comprehensive characterization. Structural analysis was conducted using X-ray diffraction (Malvern Panalytical

Empyrean, with $\text{CuK}\alpha$ radiation in the range of $10^\circ \leq 2\theta \leq 80^\circ$) to determine the crystalline phases and crystallographic properties. The morphological characteristics of the pellets formed using a hydraulic press under a pressure of $2000\text{ kg}/\text{m}^3$ were evaluated using scanning electron microscopy (Thermo Fisher Scientific Quattro ESEM). Fourier-transform infrared spectroscopy (PerkinElmer Spectrum Two instrument) was employed for spectroscopic analysis, enabling the identification of molecular vibrations and functional groups present in the synthesized perovskite. Lastly, the degradation kinetics of MB under sunlight irradiation were investigated using UV-visible spectroscopy (PerkinElmer Lambda 35 UV/Vis Spectrometer), offering insights into the photocatalytic performance of the synthesized materials. Fig. 1 illustrates the stepwise synthesis and characterization of a $x\%$ ZW-BT photocatalyst under the solar irradiation.

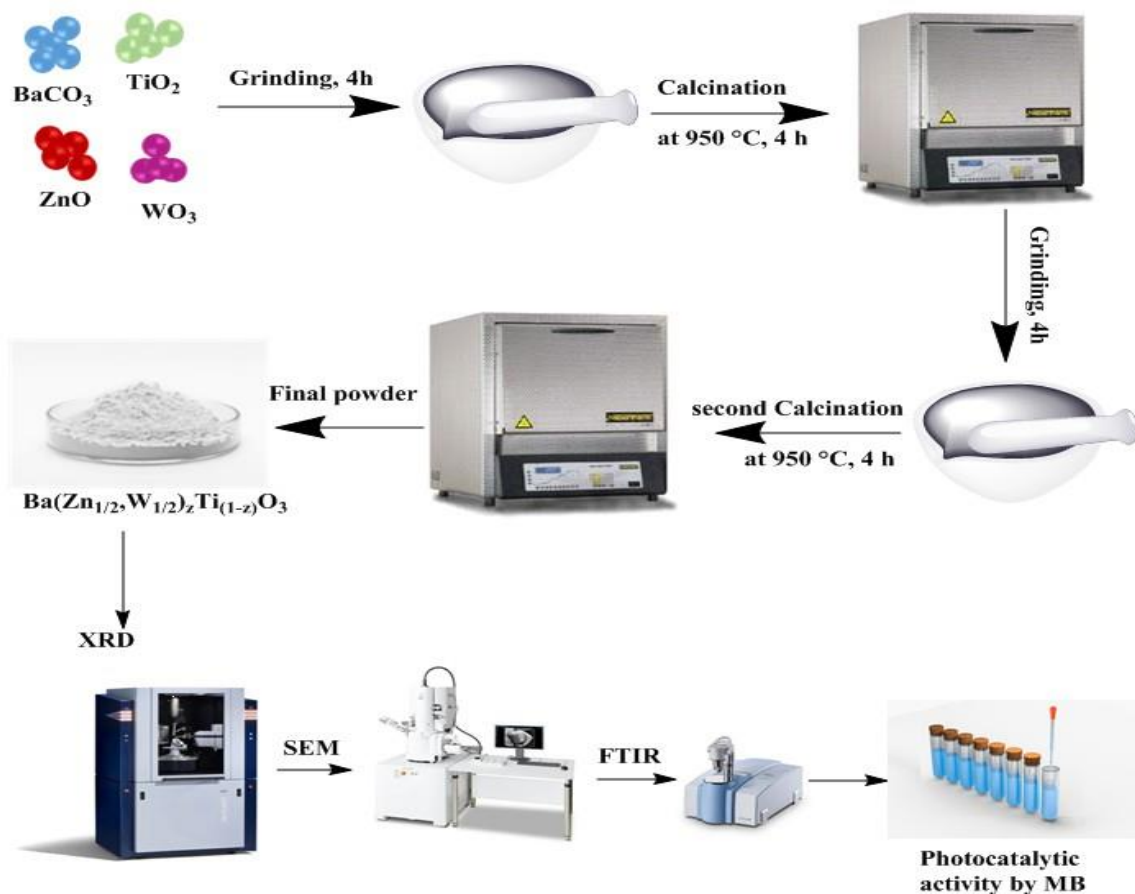


Fig. 1: The Steps of Conventional Synthesis and Characterization of $x\%$ ZW-BT Nanoparticles.

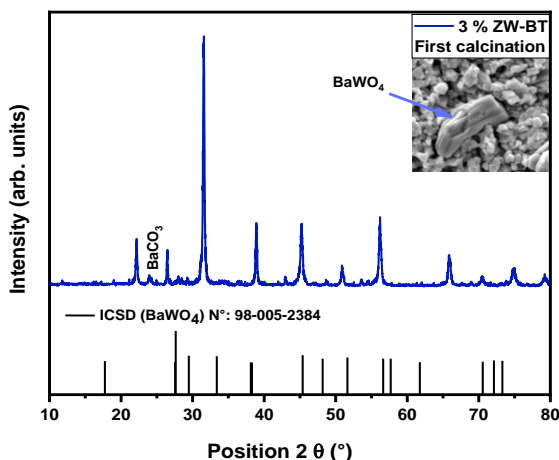


Fig. 2: X-ray diffraction patterns of 3% ZW-BT after first calcination at 950°C.

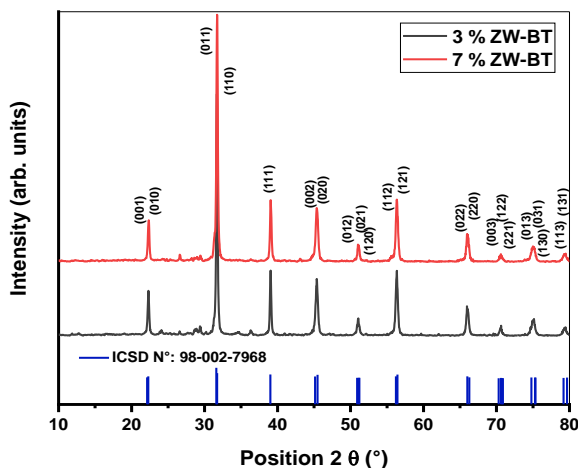


Fig. 3: X-ray Diffraction Patterns of indexed 3% and 7% ZW-BT after recalcination at 950°C.

Result and Discussion

Structural Analysis

The crystal purity of the x% ZW-BT composition, subjected to double calcination at 950°C, was assessed through X-ray diffraction (XRD) analysis. The resulting diffractograms were processed using the High Score Plus software. The purpose of the double calcination was to prevent the formation of the parasitic BaWO₄ phase and the excess of BaCO₃, as

shown in Fig. 2. Examination of the diffractogram in Fig. 3 reveals that both the 3% and 7% BZWT compositions exhibit tetragonal symmetry without any presence of parasitic phases. The majority of diffraction peaks for these compositions can be indexed to the parameters of a tetragonal cell, akin to that of BaTiO₃ (ICSD N° 98-002-7968), as illustrated by their respective (hkl) planes in Fig. 3.

The calculated lattice parameters (a)=(b) and (c) for both compositions exhibit a slight reduction with increasing dopant concentration. This reduction is accompanied by a distortion along the (c)-axis of the lattice, confirming the homogeneous diffusion of Zn²⁺ (0.47 Å) and W⁶⁺ (0.6 Å) ions. These ions partially replace Ti⁴⁺ at site B within the perovskite structure, due to their ionic radii closely resembling that of Ti⁴⁺ (0.605 Å)[19]. The lattice parameters, degree of tetragonality, and volume for the two compositions are summarized in Table 1. These values are calculated based on the interplanar distances (dhkl) provided directly by the High Score Plus software.

Furthermore, we employed X-ray diffraction data to determine the average [20], as demonstrated in equation (1):

$$D_{Scherrer} = \frac{k \times \lambda}{FWHM \times \cos \theta} \quad (1)$$

where: $D_{Scherrer}$ represents the crystallite size attributed to the analyzed peak; k is the instrumental broadening correction factor (approximately 0.9); λ signifies the wavelength of the X-ray radiation used; FWHM is the full-width at half-maximum of the diffraction peak at angle θ .

By specifically applying this method to the (110) peak and following the approach outlined by El Ghandouri *et al.* [21], we determined calculated average crystallite sizes of 47.34 nm and 56.31 nm for the 3% and 7% ZW-BT compound, respectively. These calculated sizes show a significant correlation with the experimental pellet density, which was determined using the Archimedes' method and presented in Table 1. Notably, the composition containing 7% ZW-BT, characterized by larger crystallites, demonstrates a density of 3.43 g/cm³. Conversely, the 3% ZW-BT composition exhibits a slightly lower density of 3.32 g/cm³, which coincides with the reduction in average crystallite size.

Table-1: Lattice Parameters and Density of x% ZW-BT Compositions.

x% ZW-BT	a= b	c	c/a	V(Å ³)	Position (2θ) (110)	D _{Scherrer} (nm)	Théoriques density (g/cm ³)	experimental density (g/cm ³)
0 % ZW-BT (98-002-7968)	3.986	4.014	1.0070	63.77	31.721	-	6.00	-
3 % ZW-BT	3.9850	4.0046	1.0049	63.59	31.6807	47.34	7.378	3.32
7 % ZW-BT	3.9720	4.0032	1.0061	63.15	31.7158	56.31	7.497	3.43

The FTIR spectrum of the tetragonal x% ZW-BT, as shown in Fig. 4, reveals distinctive bands at 853, 993, 1007, 1073, and 1111 cm^{-1} , corresponding to the Metal-O vibration mode at site B of the Perovskite structure[22]. Additionally, a peak at 1400 and 1590 cm^{-1} corresponds to crystalline barium titanate. These FTIR results affirm the formation of x% co-doped BaTiO₃ nanoparticles, aligning well with values reported in the literature [22,23].

Morphology and Elemental Composition

The analysis of morphology and elemental composition was extended to the synthesized x% ZW-BT nanoparticles (where x = 3% and 7%) using scanning electron microscopy (SEM) and energy-dispersive X-ray spectroscopy (EDX). The SEM images obtained, as shown in Fig. 5(a, b), highlight the surface characteristics of the nanoparticles in both the

3% and 7% ZW-BT compositions. These images clearly reveal a uniform granular stacking with an average size of 0.87 μm and 1.16 μm , respectively, calculated using Fuji software for the two compositions. This is accompanied by porosity that justifies the experimental density values for each respective composition.

The EDX spectrum displayed in Figure 5(c, d) for the x% ZW-BT nanomaterials demonstrates the presence of oxygen, barium, zinc, tantalum, and titanium as the exclusive constituents within the compound matrices across various compositions. The absence of EDX peaks corresponding to supplementary elements corroborates the exceptional crystallinity and purity of the doped barium titanate phase.

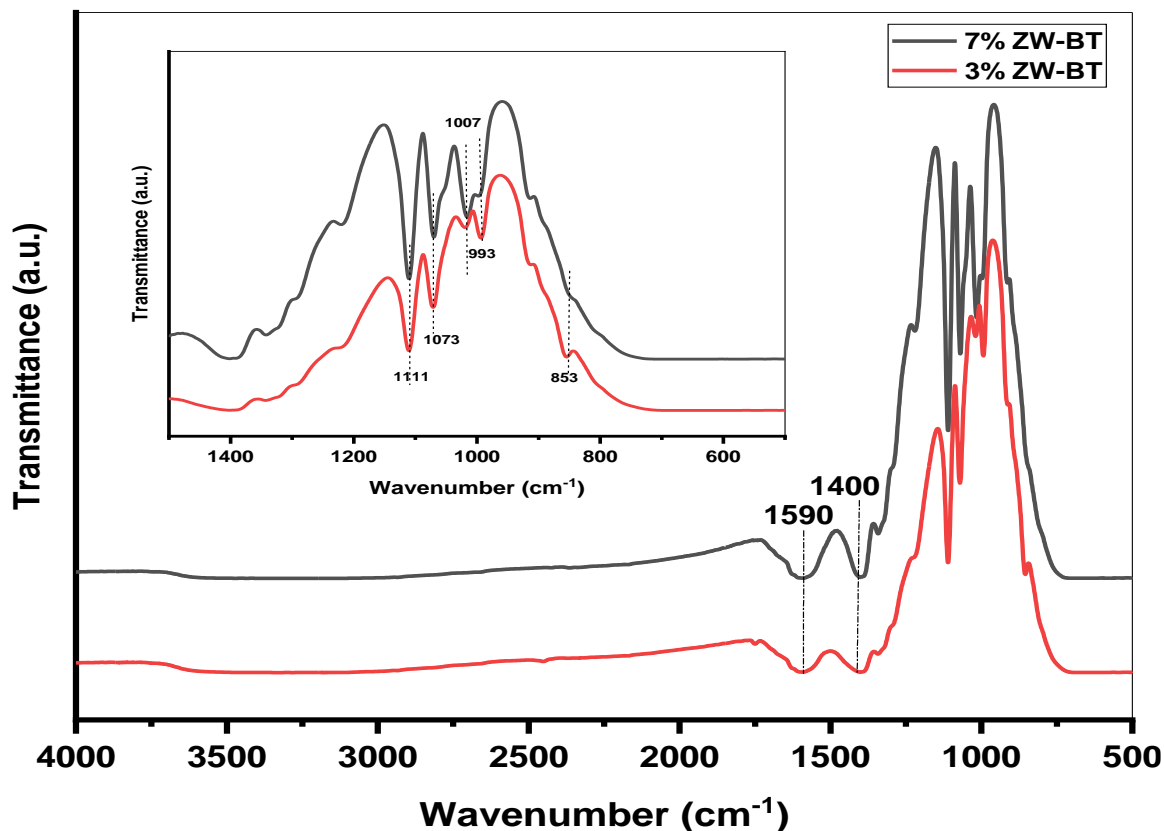


Fig. 4: FTIR Spectrum of x% ZW-BT nanoparticles

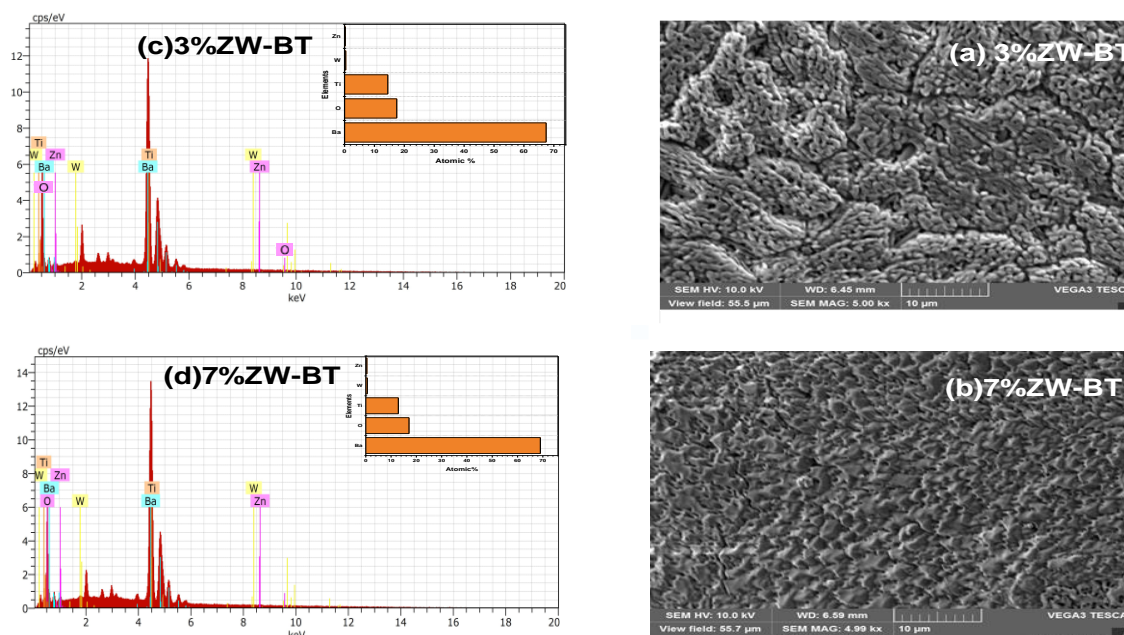


Fig. 5: (a- b) SEM images and, (c, d) EDX spectra and atomic % obtained on the x%ZW- BT sample recalcined at 950 °C.

Photocatalytic Evaluation

In the context of examining photocatalytic activity, catalysts x%ZW-BT (x=3% and 7%) were utilized, each weighing 100 mg. These catalysts were introduced into a solution containing methylene blue dye (MB) with a volume of 100 ml and a concentration of 10 mg.l^{-1} . The experimentation took place under the influence of solar radiation in March, within the Biskra region of Algeria. To establish a balanced state of adsorption and desorption, the mixture was stirred in darkness for a duration of 30 minutes. The experimental setup included the extraction of 4 mL samples from the reaction solution at 20-minute intervals during solar exposure. These samples were then subjected to centrifugation at a rate of 3000 rpm, followed by filtration. Subsequent to these steps, the filtrates underwent analysis using UV-visible spectroscopy, with readings taken at a wavelength of 664 nm. The degradation efficiency was evaluated using the following formula (Equation 2):

$$R_{\text{MB}}(\%) = \frac{(C_0 - C_t)}{C_0} \times 100 \% \quad (2)$$

where; C_0 (mg/l) represents the initial concentration of MB, and C_t (mg/l) is the concentration of the collected quantities after centrifugation. Figure 6(a, b) displays the degradation curves of x% ZW-BT during photocatalysis under sunlight irradiation. Over a span of 100 minutes, 3% and 7% ZW-BT exhibited notable degradation rates of 78.04% and 88.9%, respectively. This remarkable degradation occurred within the specified 100 min timeframe. The rate constants for these samples were computed using the equation $-\ln [C_t/C_0] = kt$ [32], which indicates adherence to pseudo-first-order kinetics[23,24]. The calculated rate constant values were 0.00998 min^{-1} for 3% ZW-BT and 0.0187 min^{-1} for 7% ZW-BT (Figure 6(c,d)).

Furthermore, distinctive peaks associated to MB remained constant and did not shift during irradiation. This constancy in peak positions signifies complete degradation of the dye into H_2O , CO_2 , and mineral salts[25,26].

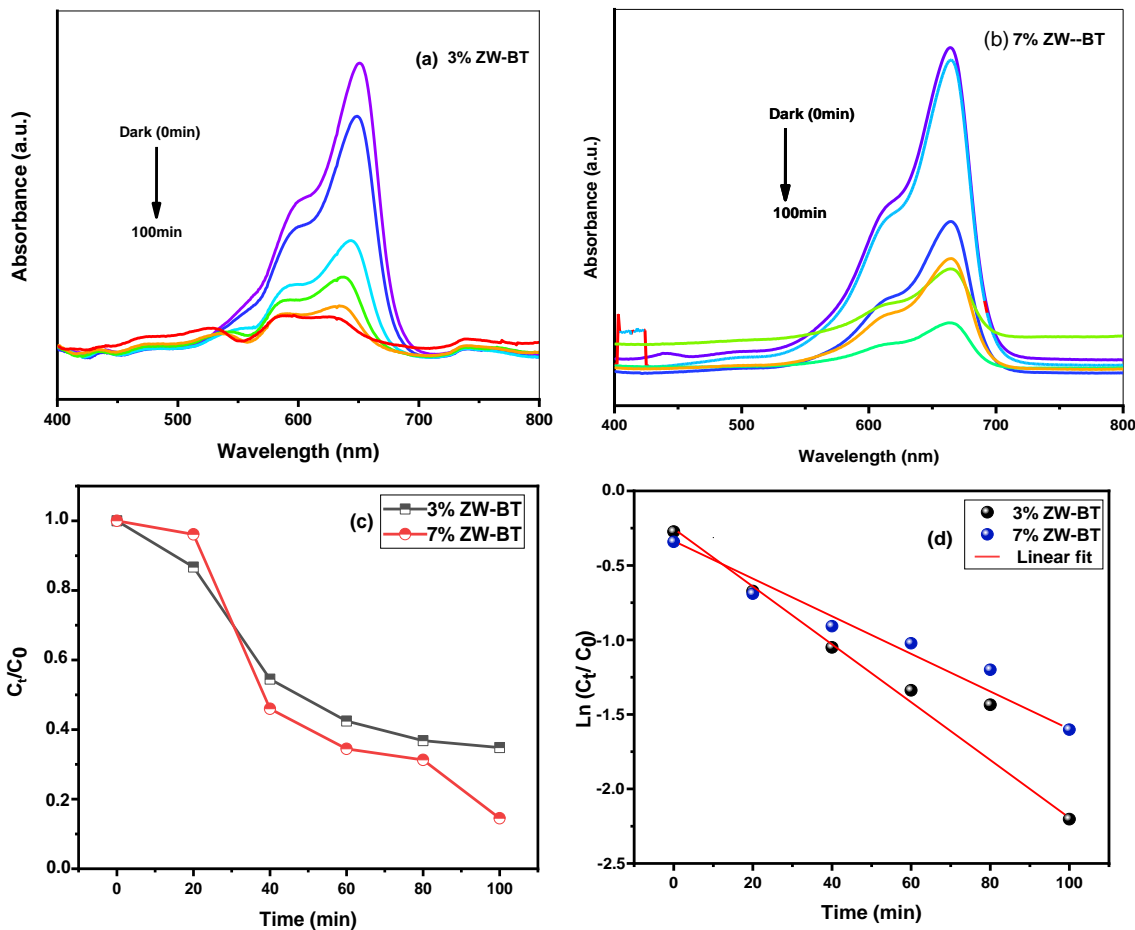


Fig. 6: (a, b) The UV–visible absorption, (c) Photocatalytic degradation of MB under Solar Irradiation: (C_t/C_0) vs. Time (T) and (d) Linear plots for pseudo-first order kinetics in the Presence of X% ZW-BT as Photocatalyst,

Thus, the degradation mechanism for x% ZW-BT catalysts during photocatalysis under solar irradiation can be elucidated through a series of reaction steps[25,27]. Initially, (x% ZW-BT) catalysts act as active surface sites. Under sunlight irradiation, electrons are excited into the conduction band, generating reactive electron species. In the first step, these reactive electron species reduce dissolved oxygen molecules (O_2) to form superoxide radicals ($\cdot O_2^-$). These superoxide radicals serve as potent oxidizing agents and initiate attacks on carbon-carbon and carbon-nitrogen bonds present in MB dye molecules. This attack leads to the fragmentation of dye molecules, generating highly reactive intermediate products. The intermediate products then undergo a sequence of degradation reactions, including hydroxylation, decarboxylation, and bond cleavage, facilitated by hydroxyl radicals ($\cdot OH$) generated through water photolysis. These reactions result in the transformation of intermediate products

into simpler compounds such as CO_2 , H_2O , and mineral salts.

Fig. 7(a) provides an illustration of the mechanism, shedding light on the process through the calculation of the conduction band (CB) and valence band (VB) potentials of x% ZW-BT. This calculation is guided by the following equations [28,29]:

$$E_{VB} = \chi - E_e + E_g/2 \quad (3)$$

$$E_{CB} = E_{VB} - E_g \quad (4)$$

where χ is the absolute electronegativity of the semiconductor, E_e is the energy of free electrons on the hydrogen scale (approximately 4.5 eV) [28], and E_g is the experimental energy of the band gap for 3% ZW-BT (2.98 eV) and 7% ZW-BT (3.19 eV). It is noteworthy that the band gap energy of x% ZW-BT compositions is calculated using the analytical model proposed by Wood and Tauc employing a direct transition method [29]. The curve of $(\alpha h\nu)^2$ against $(h\nu)$

in Fig. 7(b), when plotted, resulted in an estimated bandgap energy as previously mentioned (2.98 eV and 3.19 eV). Importantly, these values closely align with the bandgap of undoped BaTiO₃, recently reported as 3.1 eV and 3.2 eV [24,30].

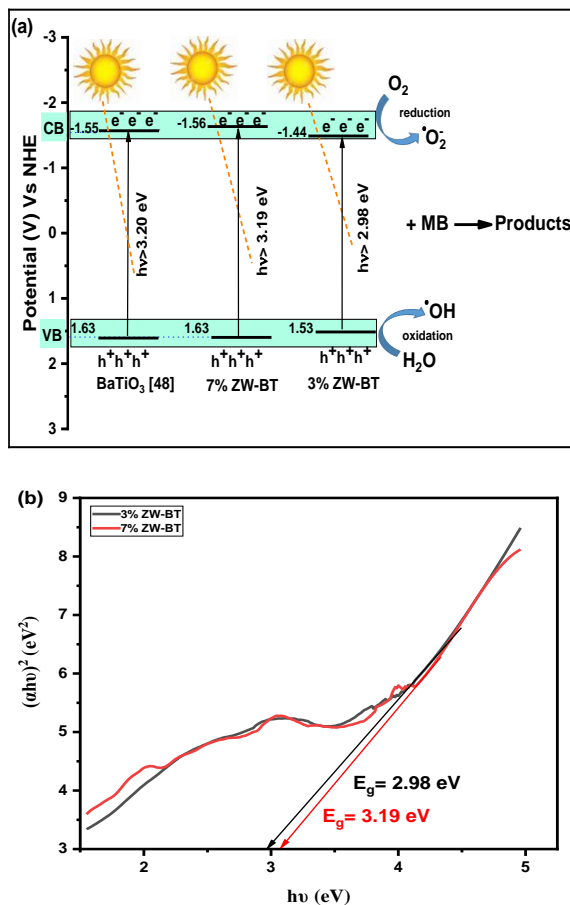


Fig. 7: (a) Schematic illustration of the photocatalytic mechanism in the x% ZW-BT photocatalyst under UV Sunlight irradiation, (b) Curve fitting of $(\alpha h\nu)^2$ vs. $(h\nu)$ using the Wood and Tauc model for x% ZW-BT nanomaterial.

Conclusion

This study investigates the characteristics of x% ZW-BT compounds ($x=3\%$ and 7%) through structural, morphological, and photocatalytic analyses synthesized via solid-state reaction. X-ray diffraction analysis confirms the crystal structure of the x% ZW-BT compositions, revealing a tetragonal symmetry devoid of parasitic phases. The lattice parameters exhibit a slight reduction with increased dopant concentrations, indicative of homogeneous dopant ion diffusion. Scanning electron microscopy (SEM) and energy-dispersive X-ray spectroscopy (EDX) reveal uniform

granular stacking and distinct elemental signatures in both compositions. The calculated crystallite sizes align well with experimental densities. Notably, photocatalytic tests showcase remarkable degradation rates, with 3% and 7% ZW-BT achieving degradation of 78.04% and 88.9%, respectively, within 100 minutes. These findings underscore the significant potential of these compounds for environmental photocatalytic applications.

Acknowledgements

The authors would like to thank Mrs. Hdjaidji Ikbal of industrial chemistry department, Biskra University, for her help with the UV-visible measurements.

References

1. F.A. Jan, R. Ullah, U. Shah, M. Saleem, N. Ullah, M.J.J.o.t.C.S.o.P. Usman, Characterization of Alpha Bismuth Trioxide Nanoparticles and their Application for Catalytic Degradation of Xylene Cyanol FF Dye in Aqueous Solution, **43** (2021).
2. G. Abderezak, O.J.J.o.t.C.S.o.P. Mahmoud, Synthesis and Characterization of Perovskite Type $\text{La}_{1-x}\text{Sr}_x\text{AlO}_{3-\delta}$ ($0 \leq X \leq 0.3$) by Co-Precipitation Method, **37** (2015).
3. P. Nayak, S.K. Nayak, Doping effect of Fe, Co and W on the structural, electrical and magnetic properties of BaTiO₃ ferroelectric ceramics, Solid State Communications, **371**, 115272 (2023).
4. J. Li, X. Qi, K. Li, M. Lu, Z. Yu, D. Wang, S. Xu, E. Sun, Z. Zhang, Abnormal mechanism of infrared fluorescence intensities in multiple phase transitions of $\text{Li}^+/\text{Er}^{3+}:\text{BaTiO}_3$ ferroelectric ceramics, Applied Physics Letters, **122**, 052902 (2023).
5. S. Assavachin, F.E. Osterloh, Ferroelectric Polarization in BaTiO₃ Nanocrystals Controls Photoelectrochemical Water Oxidation and Photocatalytic Hydrogen Evolution, Journal of the American Chemical Society, (2023).
6. J. Chen, B. Cui, J.E. Daniels, J. Wang, Q. Gu, Y. Jiang, Z. Cheng, J. Cheng, S. Zhang, Understanding the strain mechanisms in BiFeO₃-BaTiO₃ piezoelectric ceramics near the morphotropic phase boundary, Journal of the European Ceramic Society, **43**, 4766 (2023).
7. K. Liu, Y. Sun, H. Sun, Y. Du, C. Sun, Y. Shi, C. Yan, Effect of particle grading on the properties of photosensitive slurry and BaTiO₃ piezoelectric ceramic via digital light processing 3D printing, Journal of the European Ceramic Society, **43**, 3266 (2023).
8. D. Issam, M. Achehboune, I. Boukhoubza, R. Hatel, Z. El Adnani, A. Rezzouk, Investigation of the crystal structure, electronic and optical properties of Cr-doped BaTiO₃ on the Ti site using first principles

- calculations, *Journal of Physics and Chemistry of Solids*, **175**, 111209 (2023).
- H. Shen, K. Xia, P. Wang, R. Tan, The electronic, structural, ferroelectric and optical properties of strontium and zirconium co-doped BaTiO₃: First-principles calculations, *Solid State Communications*, **355**, 114930 (2022).
 - M.V. Kaushik, M. Kumar, A. Kumar, Structural and Optical Properties of BaTiO₃ Thin Film Deposited on Quartz Substrate by Sol Gel Technique, (2023).
 - D. Masekela, N.C. Hintsho-Mbita, S. Sam, T.L. Yusuf, N. Mabuba, Application of BaTiO₃-based catalysts for piezocatalytic, photocatalytic and piezo-photocatalytic degradation of organic pollutants and bacterial disinfection in wastewater: A comprehensive review, *Arabian Journal of Chemistry*, 104473 (2022).
 - Q. Zhang, Y. Jia, W. Wu, C. Pei, G. Zhu, Z. Wu, L. Zhang, W. Fan, Z. Wu, Review on strategies toward efficient piezocatalysis of BaTiO₃ nanomaterials for wastewater treatment through harvesting vibration energy, *Nano Energy*, **113**, 108507 (2023).
 - W. Qian, H. Wu, Y. Yang, Ferroelectric BaTiO₃ Based Multi-Effects Coupled Materials and Devices, *Advanced Electronic Materials*, **8**, 2200190 (2022).
 - S. Chang, C. Chen, X. Jiang, C. Zhao, J. Chen, Improved chemical defects, domain structure and electrical properties of BiFeO₃-BaTiO₃ lead-free ceramics by simultaneous Na/Bi codoping and quenching process, *Ceramics International*, **49**, 16191 (2023).
 - A. Prasatkhetragarn, T. Sareein, N. Triamnak, R. Yimnirun, Dielectric and ferroelectric properties of modified-BaTiO₃ lead-free ceramics prepared by solid solution method, *Ferroelectrics*, **586**, 224 (2022).
 - H. Gouadria, M. Smari, T. Mnasri, J. Necib, J.L. Sánchez, P. Marín, A.P. Jamale, R.B. Younes, Implementing a sol-gel route to adjust the structural and dielectric characteristics of Bi and Fe co-doped BaTiO₃ ceramics, *Inorganic Chemistry Communications*, 110241 (2022).
 - R. Jana, P.M. Rajaiitha, S. Hajra, H.J. Kim, Advancements in visible-light-driven double perovskite nanoparticles for photodegradation, *Micro and Nano Systems Letters*, **11**, 3 (2023).
 - S. Yakout, Influence of Na and Na/Fe doping on the dielectric constant, ferromagnetic and sunlight photocatalytic properties of BaTiO₃ perovskite, *Journal of Solid State Chemistry*, **290**, 121517 (2020).
 - M. Staruch, H. ElBidweihy, M. Cain, P. Thompson, C. Lucas, P. Finkel, Magnetic and multiferroic properties of dilute Fe-doped BaTiO₃ crystals, *APL Materials*, **8** (2020).
 - J. Chen, H. Deng, Y. Pan, D. Zheng, L. Sun, J. Tao, P. Yang, J. Chu, Band gap modulation and improved magnetism of double perovskite Sr₂KMoO₆ (K= Fe, Co, Ni, Mn) doped BaTiO₃ ceramics, *Ceramics International*, **48**, 7629 (2022).
 - A. Semenov, A. Dedyk, I. Mylnikov, O. Pakhomov, A. Es'kov, A. Anokhin, V. Krylov, A. Burovikhin, Y. Pavlova, A. Tselev, Mn-doped BaTiO₃ ceramics: Thermal and electrical properties for multicaloric applications, *Materials*, **12**, 3592 (2019).
 - A. Madani, M. Alghamdi, B. Alamri, S. Althobaiti, Structural and optical properties of Sb-BaTiO₃ and Y-BaTiO₃ doped ceramics prepared by solid-state reaction, *Optical Materials*, **137**, 113480 (2023).
 - B. Yang, H. Chen, Y. Yang, L. Wang, J. Bian, Q. Liu, X. Lou, Insights into the tribo-/pyro-catalysis using Sr-doped BaTiO₃ ferroelectric nanocrystals for efficient water remediation, *Chemical Engineering Journal*, **416**, 128986 (2021).
 - S. More, M.V. Khedkar, G.D. Kulkarni, P. Kadhane, R. Kamble, K. Jadhav, Effect of iron doping on structural, DC electrical resistivity and ferroelectric properties of BaTiO₃ nanoceramics, *Optik*, **247**, 167913 (2021).
 - M. Tihtih, J.E.F. Ibrahim, M.A. Basyooni, R. En-Nadir, W. Belaid, I. Hussainova, I. Kocserha, Development of Yttrium-Doped BaTiO₃ for Next-Generation Multilayer Ceramic Capacitors, *ACS omega*, **8**, 8448 (2023).
 - P.P. Khirade, A.V. Raut, Perovskite Structured Materials: Synthesis, Structure, Physical Properties and Applications, in: *Recent Advances in Multifunctional Perovskite Materials*, IntechOpen, (2022).
 - S. More, M. Khedkar, S. Jadhav, S.B. Somvanshi, A. Humbe, K. Jadhav, Wet chemical synthesis and investigations of structural and dielectric properties of BaTiO₃ nanoparticles, in: *Journal of Physics: Conference Series*, IOP Publishing, pp. 012007 (2020).
 - C. Tian, Z. Yue, Y. Zhou, L. Li, Crystal structures and microwave dielectric properties of Zn,W co-substituted BaTiO₃ perovskite ceramics, *Journal of Solid State Chemistry*, **197**, 242 (2013).
 - Z. Hu, V. Koval, Y. Yue, M. Zhang, C. Jia, I. Abrahams, H. Yan, Structural evolution and coexistence of ferroelectricity and antiferromagnetism in Fe, Nb co-doped BaTiO₃ ceramics, *Journal of the European Ceramic Society*, **43**, 2460 (2023).
 - S. Sahoo, A. Yadav, K. Andryushin, P. Mahapatra, R. Choudhary, Structural transformation, dielectric and multiferroic properties of (Gd_{1-x}Ba_x)(Fe_{1-x}Ti_x)O₃ ceramics by tuning composition, *Ceramics International*, **49**, 918 (2023).

31. M.S. Hossain, S.K. Das, M. Moniruzzaman, M. Hakim, M. Basith, Frequency and temperature dependent electric polarization, relaxation, and transport properties of Mo and W doped BaTiO₃, *Results in Physics*, **30**, 104873 (2021).
32. H. Ahn, E. Lee, Y. Cho, D. Bae, H.J. Park, J. Yang, J. Cho, S. Cho, Ferroelectric transition in Sr-and W-Doped BaTiO₃ solid solutions, *Applied Sciences*, **11**, 6760 (2021).
33. P. Demircivi, E.B. Simsek, Visible-light-enhanced photoactivity of perovskite-type W-doped BaTiO₃ photocatalyst for photodegradation of tetracycline, *Journal of Alloys and Compounds*, **774**, 795 (2019).
34. E. Hannachi, K. Mahmoud, M. Sayyed, Y. Slimani, Structure, optical properties, and ionizing radiation shielding performance using Monte Carlo simulation for lead-free BTO perovskite ceramics doped with ZnO, SiO₂, and WO₃ oxides, *Materials Science in semiconductor processing*, **145**, 106629 (2022).
35. A. Mishra, D.K. Khatua, A. De, R. Ranjan, Off-stoichiometry, structural-polar disorder and piezoelectricity enhancement in pre-MPB lead-free Na_{0.5}Bi_{0.5}TiO₃-BaTiO₃ piezoceramic, *Journal of Applied Physics*, **125** (2019).
36. A. Mishra, D.K. Khatua, G. Das Adhikary, N. Kumar, A. Upadhyay, B. Mahale, S. Saha, B. Majumdar, A. Senyshyn, R. Ranjan, Effect of sintering temperature on the structural disorder and its influence on electromechanical properties of the morphotropic phase boundary composition 0.94 Na_{0.5}Bi_{0.5}TiO₃-0.06 BaTiO₃ (NBT-6BT), *Journal of Materials Science: Materials in Electronics*, **32**, 16088 (2021).
37. A. Sood, A.D. Poletayev, D.A. Cogswell, P.M. Csernica, J.T. Mefford, D. Fraggedakis, M.F. Toney, A.M. Lindenberg, M.Z. Bazant, W.C.J.N.R.M. Chueh, Electrochemical ion insertion from the atomic to the device scale, **6**, 847 (2021).
38. G. Renaudin, S. Gomes, J.-M. Nedelec, First-Row Transition Metal Doping in Calcium Phosphate Bioceramics: A Detailed Crystallographic Study, **10**, 92 (2017).
39. S. Fatimah, R. Ragadhita, D.F. Al Husaeni, A.B.D. Nandiyanto, How to calculate crystallite size from x-ray diffraction (XRD) using Scherrer method, *ASEAN Journal of Science and Engineering*, **2**, 65 (2022).
40. M. Khan, A. Mishra, J. Shukla, P. Sharma, X-ray analysis of BaTiO₃ ceramics by Williamson-Hall and size strain plot methods, in: *AIP Conference Proceedings*, AIP Publishing, (2019).
41. S. Gel, Effect of strontium on the structural and piezoelectric properties of the sol gel processed barium titanate, *J. Mater. Environ. Sci*, **8**, 4945 (2017).
42. M. Fatema, A. Bajpai, A. Somvanshi, S. Manzoor, M. Arshad, N. Zarrin, A.A. Qahtan, W. Khan, S. Husain, Study of structural correlations with temperature dependent dielectric response and ferroelectric behavior for (Sr, Mn) co-doped BaTiO₃, *Journal of Materials Science: Materials in Electronics*, **33**, 6329 (2022).
43. M.K. Adak, D. Mondal, S. Mondal, S. Kar, S.J. Mahato, U. Mahato, U.R. Gorai, U.K. Ghorai, D. Dhak, Ferroelectric and photocatalytic behavior of Mn-and Ce-doped BaTiO₃ nanoceramics prepared by chemical route, *Materials Science and Engineering: B*, **262**, 114800 (2020).
44. J. Swain, A. Priyadarshini, S. Hajra, S. Panda, J. Panda, R. Samantaray, Y. Yamauchi, M. Han, H.J. Kim, R.J.J.o.A. Sahu, Compounds, Photocatalytic dye degradation by BaTiO₃/zeolitic imidazolate framework composite, **965**, 171438 (2023).
45. B. Ohtani, Photocatalysis A to Z—What we know and what we do not know in a scientific sense, *Journal of Photochemistry and Photobiology C: Photochemistry Reviews*, **11**, 157 (2010).
46. P.M. Rajaiitha, S. Hajra, M. Sahu, K. Mistewicz, B. Toroń, R. Abolhassani, S. Panda, Y. Mishra, H.J.J.M.T.C. Kim, Unraveling highly efficient nanomaterial photocatalyst for pollutant removal: a comprehensive review and future progress, **23**, 100692 (2022).
47. S.K. Ray, J. Cho, J. Hur, A critical review on strategies for improving efficiency of BaTiO₃-based photocatalysts for wastewater treatment, *Journal of environmental management*, **290**, 112679 (2021).
48. H. Menasra, Z. Necira, K. Bounab, C. Benbrika, L. Smaili, Influence of the isothermal annealing time on structural morphological, and photocatalytic characters of BiT/ZnWO₄ composite, *Digest Journal of Nanomaterials and Biostructures*, **18**, 1315 (2023).
49. G. Chen, N.H. Wong, J. Sunarso, Y. Wang, Z. Liu, D. Chen, D. Wang, G.J.A.S.S. Dai, Flexible Bi₂MoO₆/S-C₃N₄/PAN heterojunction nanofibers made from electrospinning and solvothermal route for boosting visible-light photocatalytic performance, **612**, 155893 (2023).
50. S. Asadullayeva, N. Ismayilova, N. Mamedov, A. Bayramov, M. Musayev, Q. Eyyubov, E. Kasumova, I. Afandiyeva, K.O.J.S.S.C. Sadig, Photoluminescence and density functional theory analysis of BaTiO₃: Mn, **372**, 115307 (2023).